

Active megadetachment beneath the western United States

Brian Wernicke,¹ James L. Davis,² Nathan A. Niemi,³ Peter Luffi,^{1, 4} and Sunil Bisnath,^{2, 5}



ABSTRACT
Geodetic data, interpreted in light of seismic imaging, seismicity, xenolith studies, and the Late Quaternary geologic history of the northern Great Basin, suggest that a subcontinental-scale extensional detachment is localized near the Moho. To first order, seismic yielding in the upper crust at any given latitude in this region occurs via an M7 earthquake every 100 years. Since 1996, the region has completed a cycle of strain accumulation and release similar to 'slow earthquakes' observed on subduction megathrusts, but yielding occurred on a surface 5–10 times larger in the slip direction, and at temperatures >800°C. Strain energy with moment magnitude equivalent to an M7 earthquake was released along this 'megadetachment' relatively uniformly between 2000.0 and 2004.0. Net slip was variable, ranging from 5–10 mm over most of the region. Slip initiated in late 1998 to mid-1999 in northeastern Nevada, and culminated in 2003 with a magma injection event at Moho depth beneath the Sierra Nevada, accompanied by more rapid eastward relative displacement across the entire region. Strain energy thus appears to have been transmitted from the Cordilleran interior toward the plate boundary, from high gravitational potential to low, via quasi-periodic yielding (stick-slip) on the megadetachment. Its size and mechanical function imply that lithospheric strength resides well below the seismogenic layer, even in a high heat flow tectonic regime. A strong lowermost crust and upper mantle is consistent with deformation microstructures and low water content in dunite xenoliths in young lavas in central Nevada, and with high-temperature microstructures in analog surface exposures of the lower crust. Large-scale structural disharmony between crust and upper mantle is consistent with the broad distribution of strain in the upper crust versus the more localized distribution in the subcrustal lithosphere, as inferred by such proxies as low P-wave velocity and mafic magmatism.

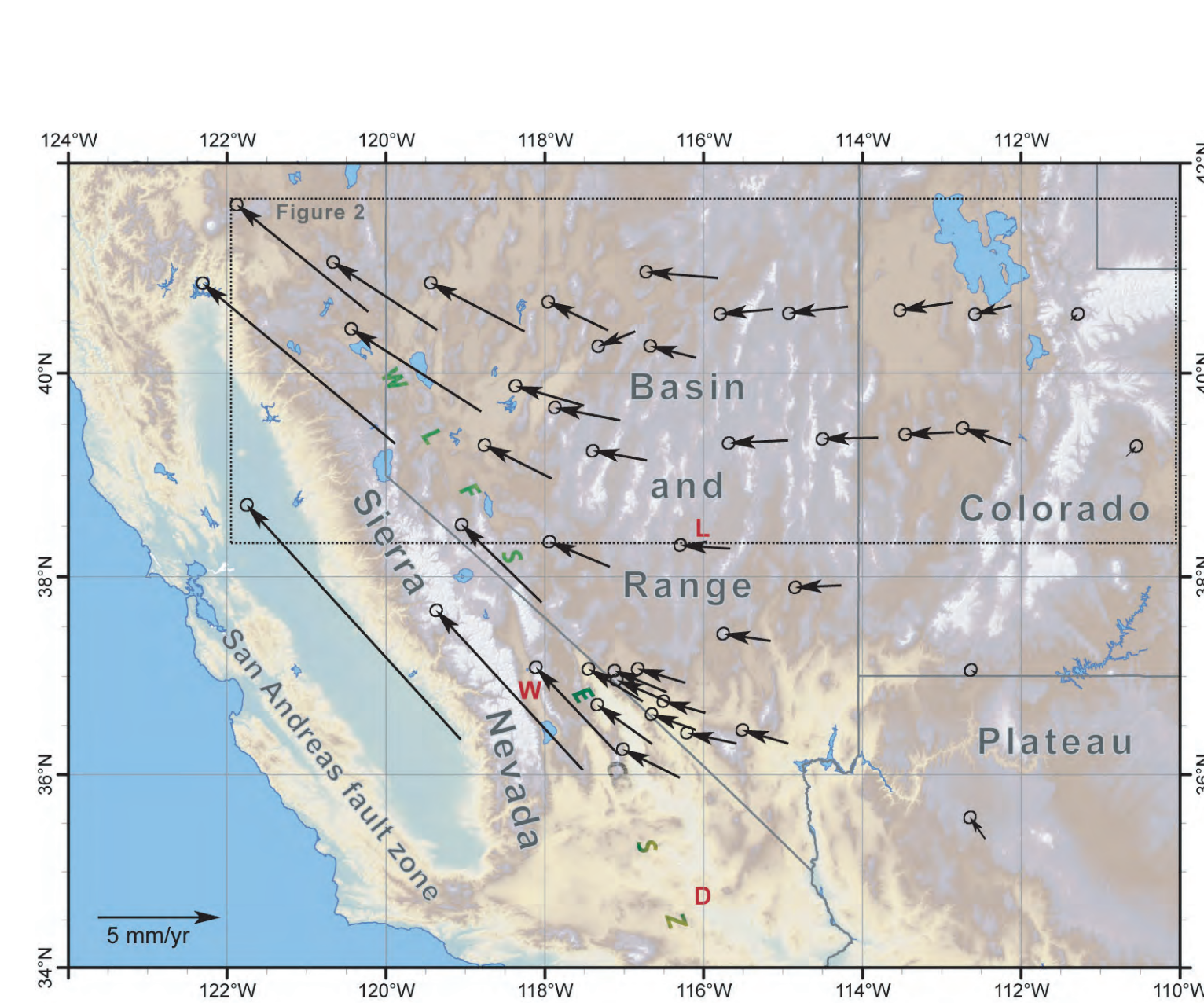


Figure 1. Colored relief map showing average BARGEN velocity field, after Davis et al., 2006 (some BARGEN site velocities near Yucca Mountain omitted to reduce clutter). Box shows location of Figure 2. WLFs, Walker Lane fault system; ECSZ, Eastern California shear zone. Red letters indicate locations of xenolith-bearing volcanic fields: D, Dish Hill, California; L, Lunar Craters, Nevada; W, Waucoba, Owens Valley area, California.

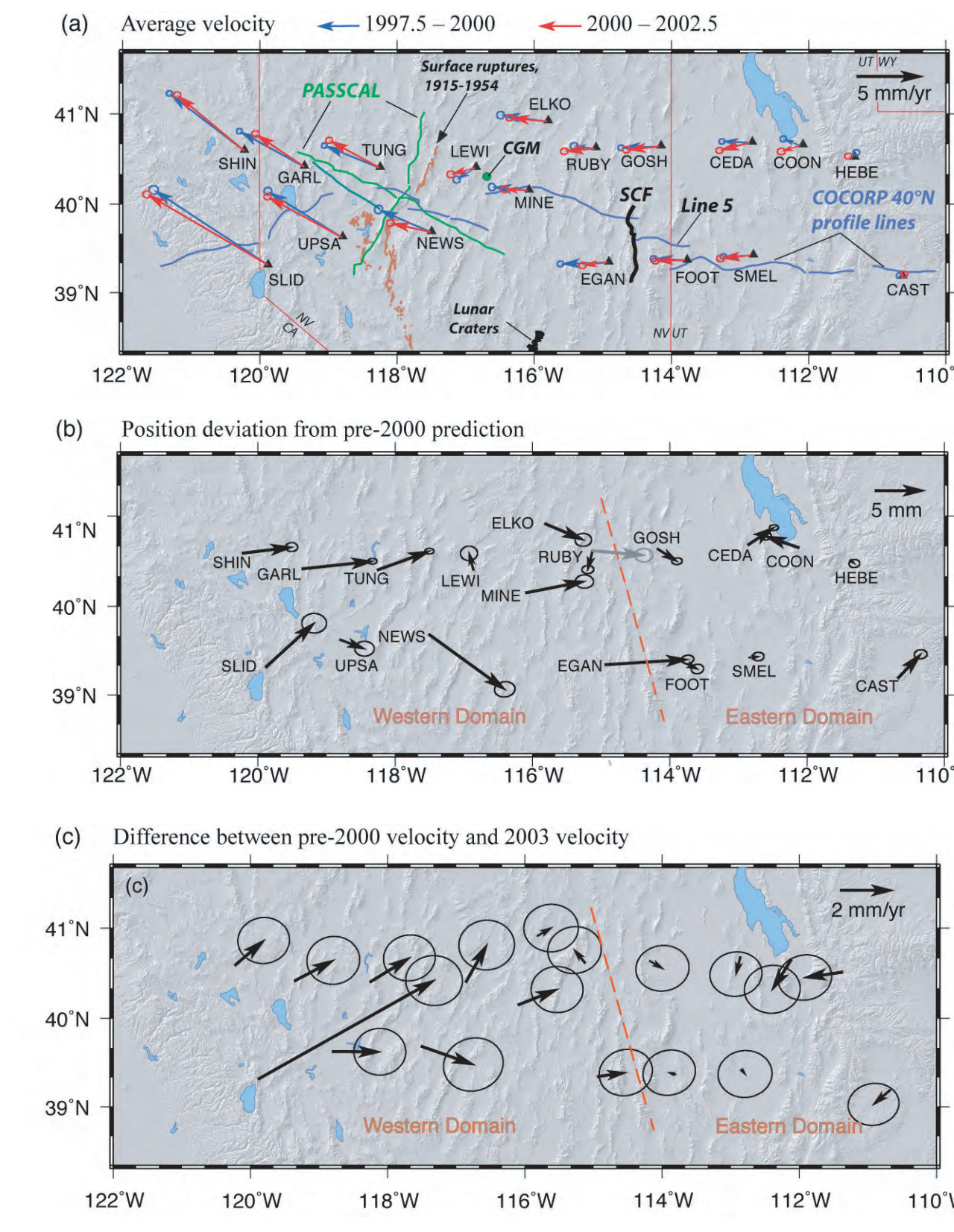


Figure 2. Map showing velocity and displacement fields associated with transient motions of the first 18 BARGEN sites installed across northern Great Basin. (a) first the geodetic network solution of Davis et al. [2006]. (a) average velocities for intervals 1997.5 to 2000.0 (blue arrows) and 2000.0 to 2002.5 (red arrows). Also shown: position of COCORP 40°N profile lines (blue), PASSCAL survey lines (green); traces of Central Nevada seismic belt surface ruptures (brown) after Bell et al. [2004]; surface trace of Schell Creek fault (SCF) and the location of Cortez Gold mine open-pit operation (CGM). (b) Deviations from position predicted on the basis of pre-2000 site velocities (Davis et al. 2006), showing approximate boundary between eastern and western geodetic domains; deviations of sites CEDA and COON have been corrected for lake loading effects (Elosegui et al. [2003] but likely still contains unmodeled hydrological signal from ground-water effects in the metropolitan area around Salt Lake City. Gray arrow for site RUBY shows deviation from pre-1998.5 estimated velocity. (c) Difference between of 2003.0 to 2004.0 velocity and 1997.5 to 2000 average velocity, similar to Figure 4b in Davis et al. [2006] but making a comparison of 2003 with a more narrow, earlier interval of time.

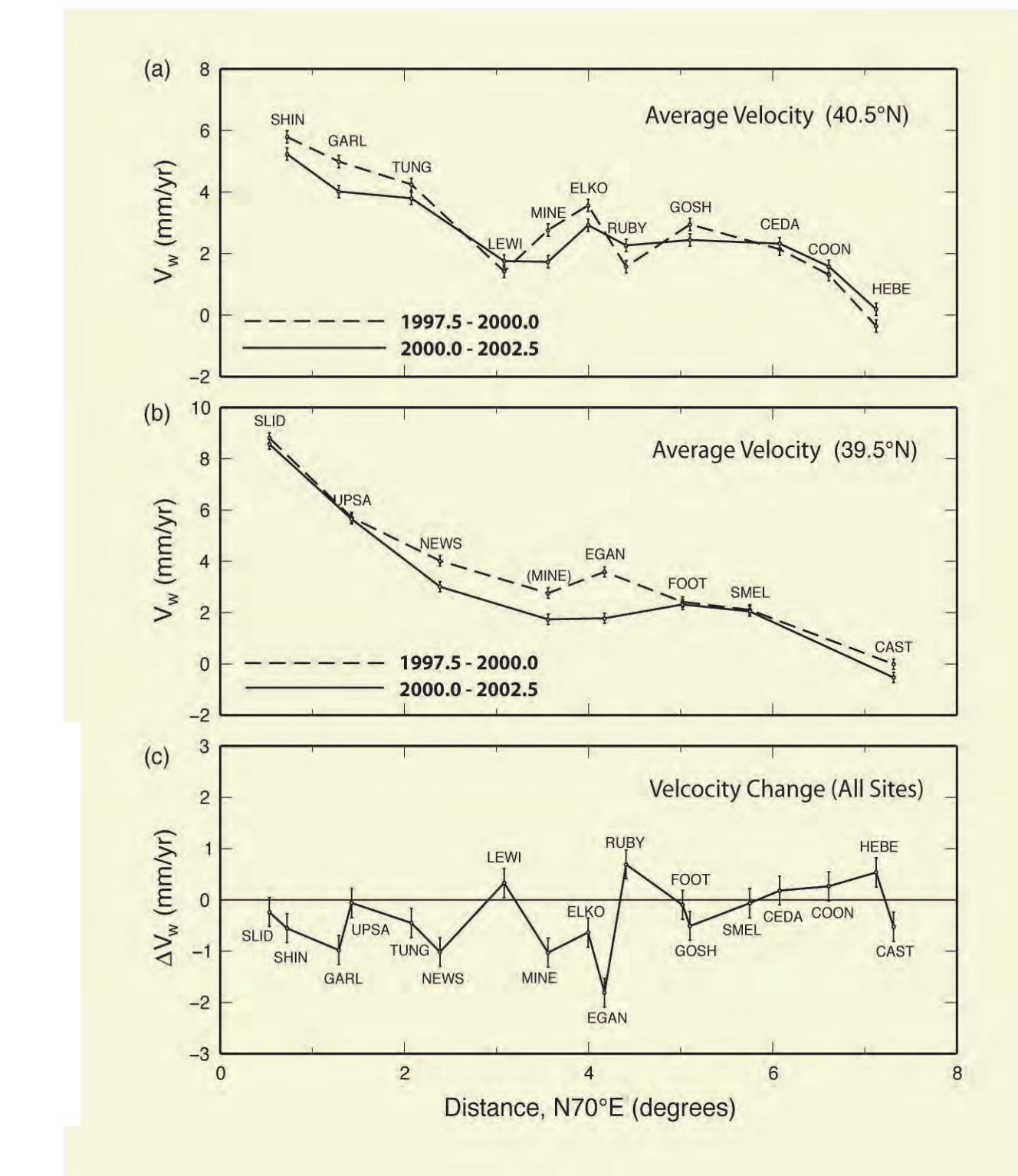


Figure 3. West component of velocity relative to North America versus position projected along N70°E. (a) northern transect; (b) southern transect, including site MINE from the northern transect; (c) difference in west component of velocity

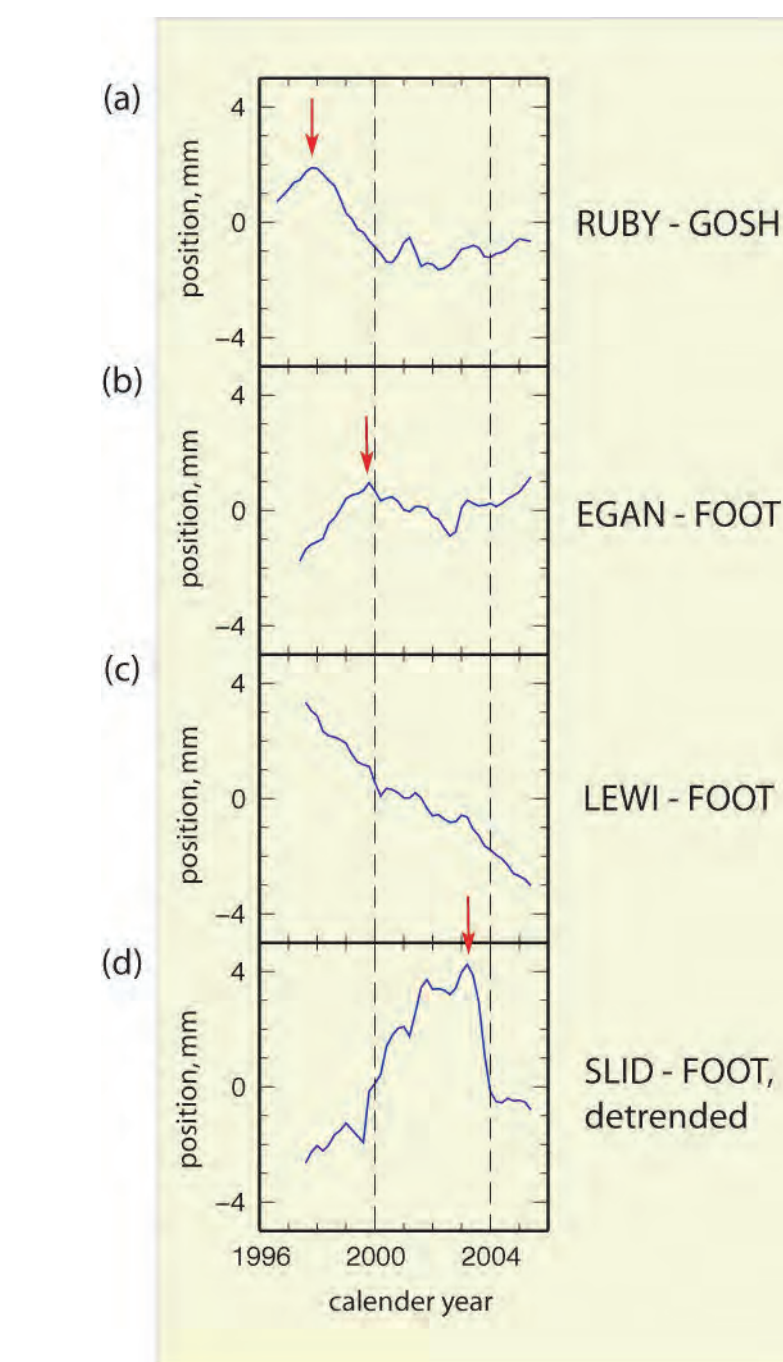


Figure 4. Filtered time series (using data and method presented in Davis et al. [2006]) of east component of baseline length for selected sites; negative slopes in (a) through (c) indicate baseline contraction, positive slopes extension (45° = 1 mm/yr). Vertical red arrows show interpreted time of onset of slowing in west velocity. Mean slope of plot in (d) has been removed.

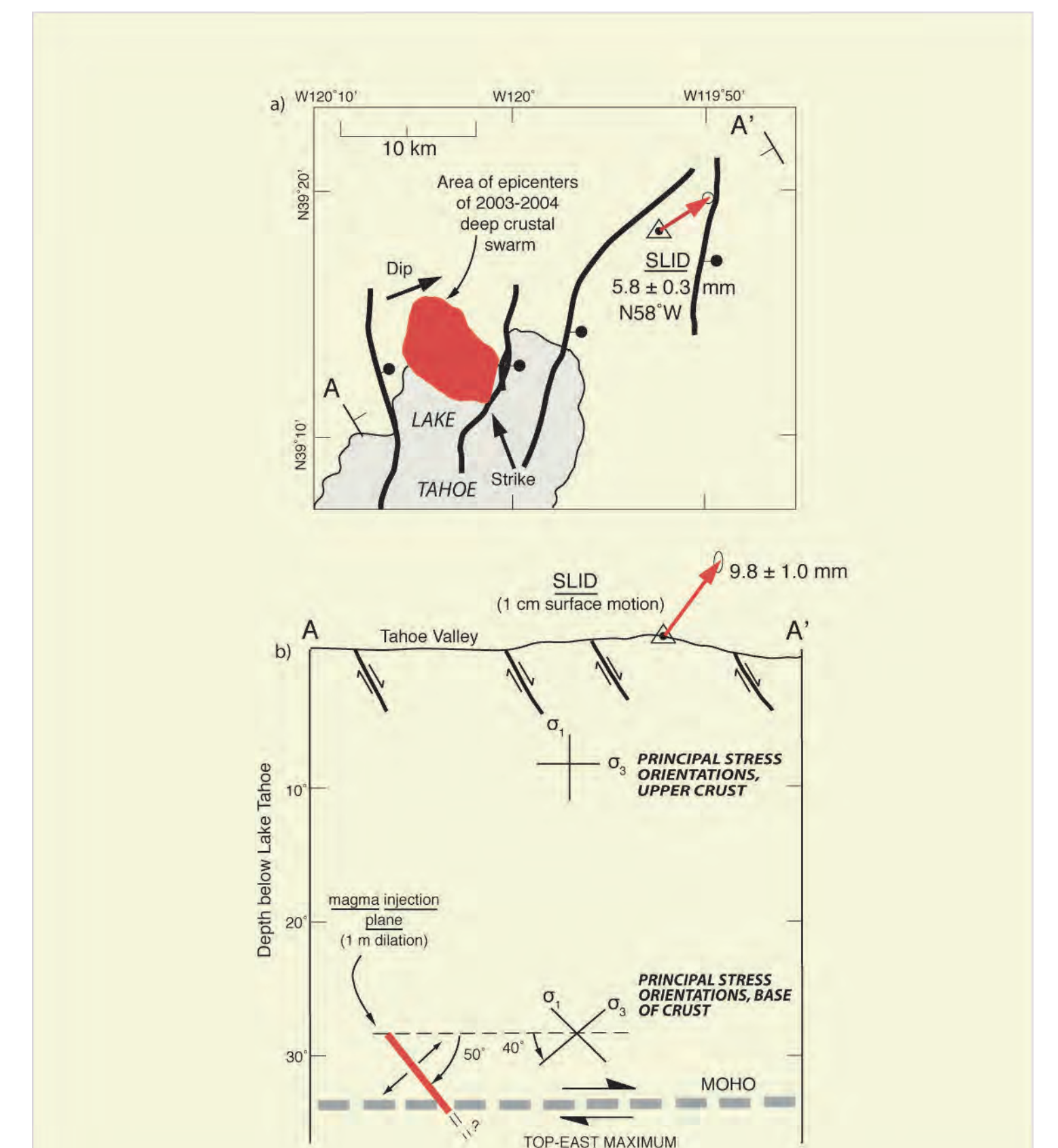


Figure 5. (a) Map showing relationship between the epicentral area of the August 2003 to February 2004 deep crustal seismic swarm and horizontal component of transient motion of site SLID (Smith et al., 2004). Heavy lines show surface traces of principal normal faults along cross section A-A'. Ball-and-bar symbol indicates downthrown side. (b) Cross section showing the magmatic injection plane inferred from the seismic swarm in relation to the total (horizontal and vertical) transient motion of site

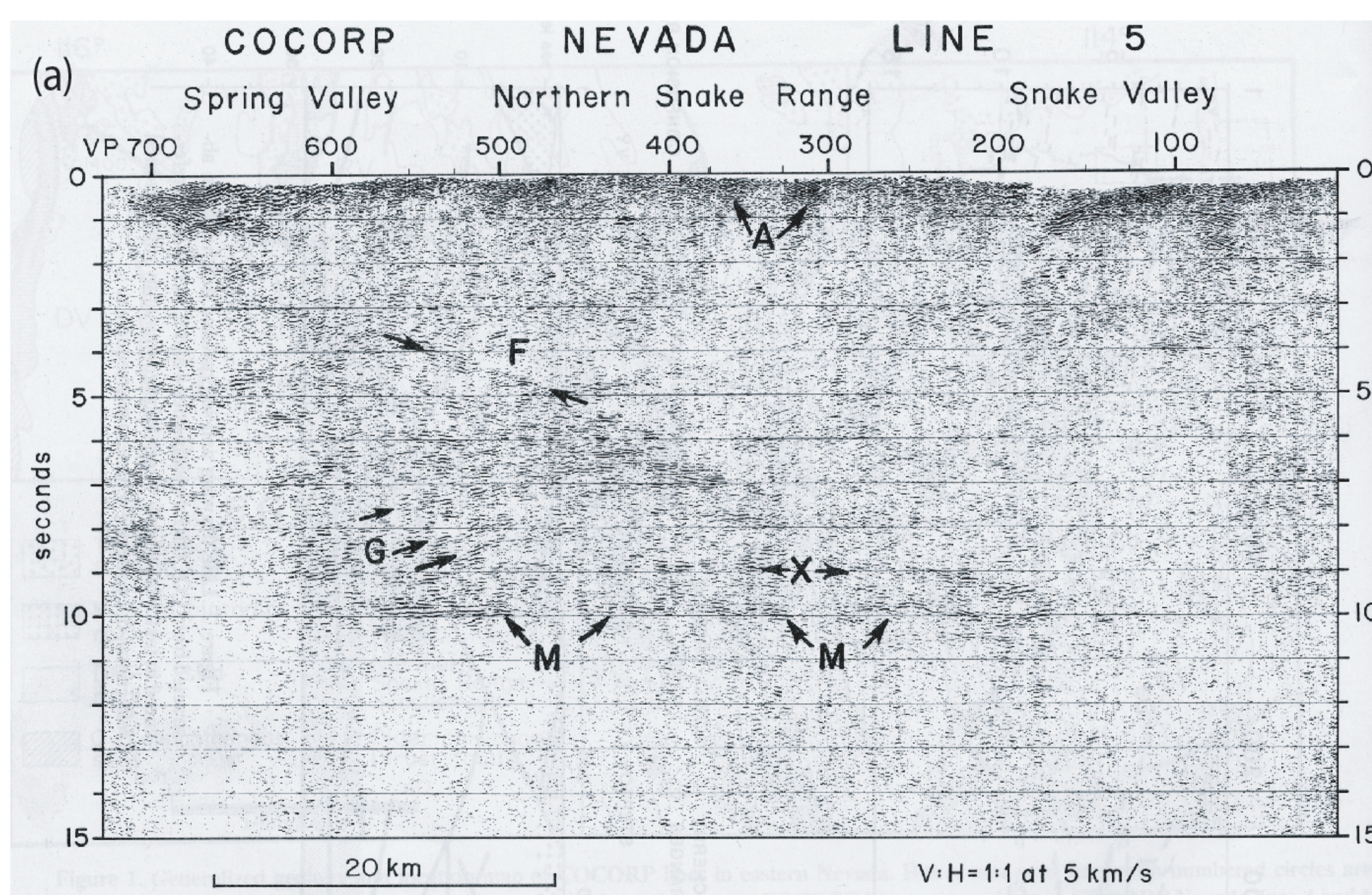


Figure 6. (a) Seismic reflection profile (COCORP Nevada Line 5) showing transition between strong Moho reflections (labeled X and M) and subhorizontal deep reflections (unlabeled reflections above X and M) characteristic of Nevada, and the west-dipping reflections (labeled G and W) characteristic of western Utah. East-dipping reflections labeled F project upward to the surface trace of the Schell Creek fault just west of VP 700, and downward along terminations of subhorizontal deep crustal reflections. From Hauser et al. [1987]. (b) Schematic east-west cross section showing interpretation of the Schell Creek fault as an active crustal-penetrating boundary against which deep crustal magmatic sills terminate. SNVY, Snake Valley; SPVY, Spring Valley; SCR, Schell Creek Range; STVY, Steptoe Valley; ER, Egan Range. From Hauser et al. [1987].

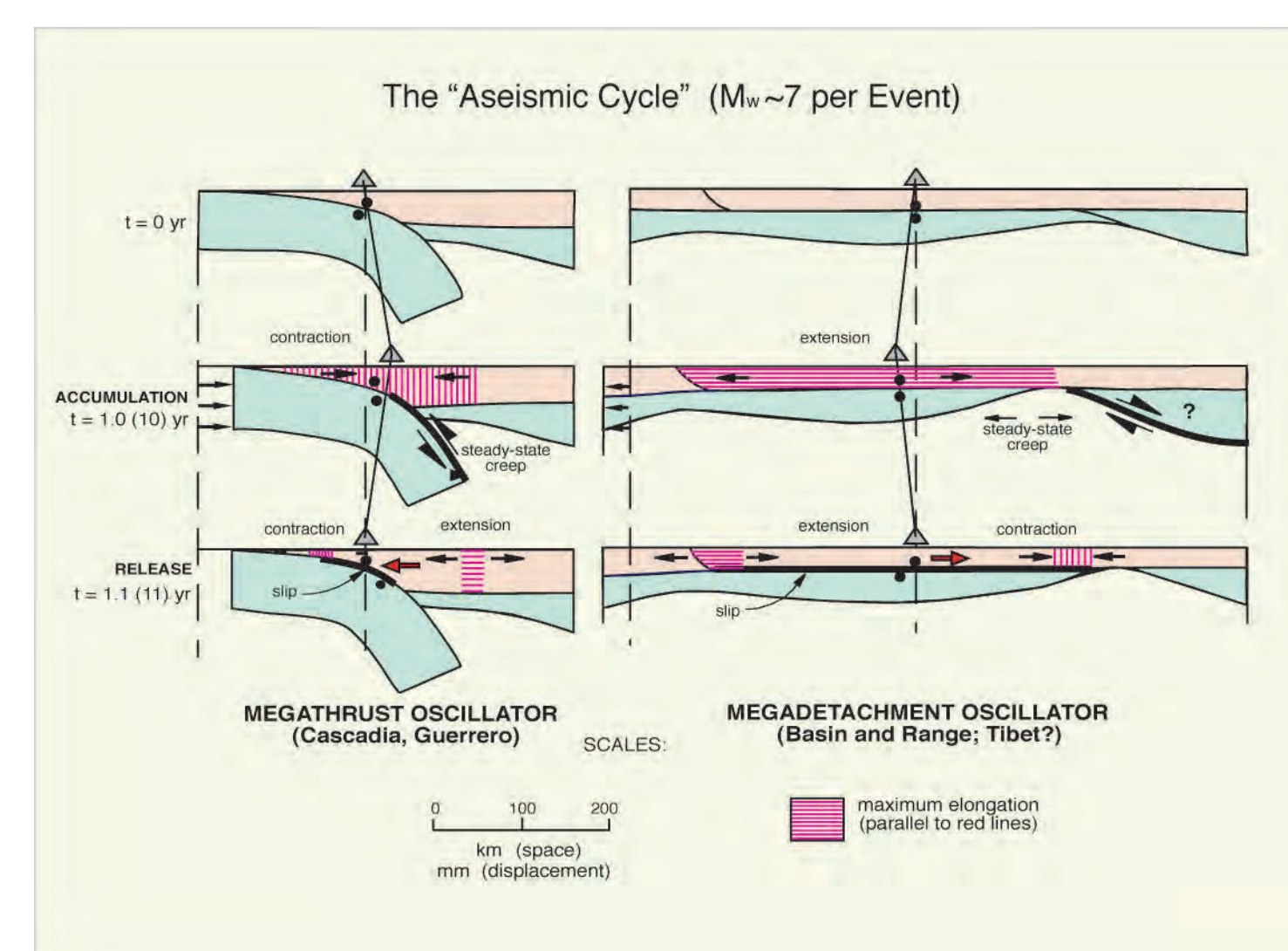


Figure 10. Schematic cross sectional models drawing analogy between top-east displacement and associated strain patterns on the megadetachment and slow earthquakes in a subduction zone setting as described in text.

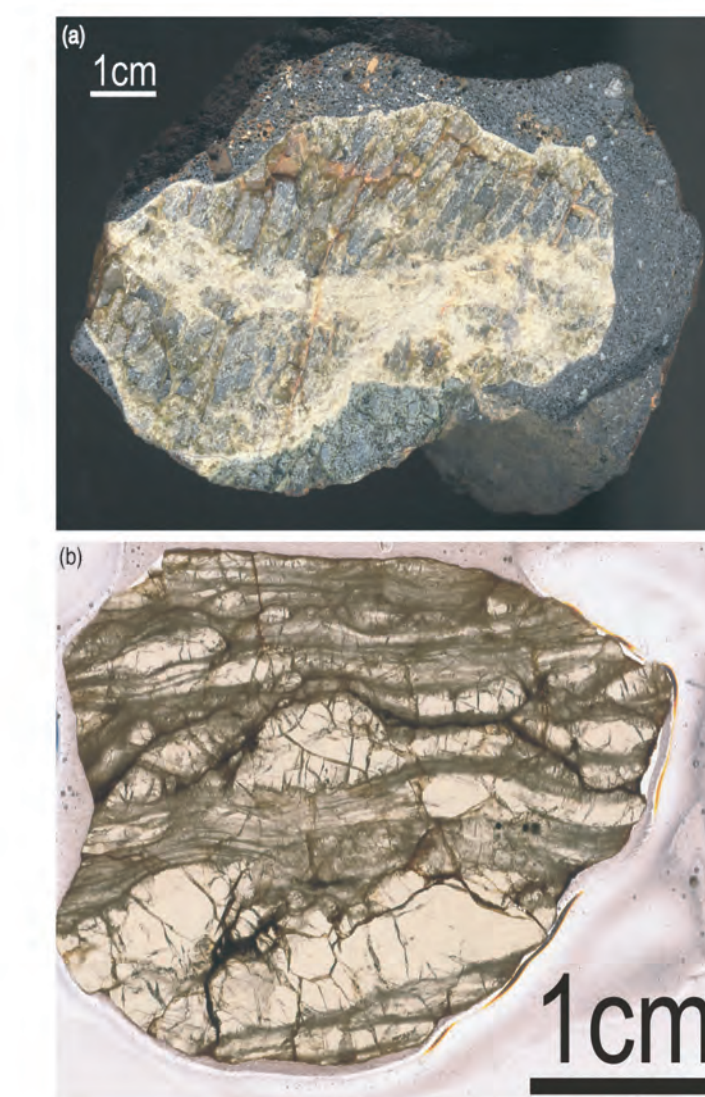


Figure 7. Representative deformation textures in dunite xenoliths from the Marath cinder cone, Lunar Craters volcanic field, Nevada (Figure 1); both samples contain 2 ppm weight percent H2O in olivine (Table 1). (a) Photograph of polished surface of sheared dunite xenolith showing strong grain size reduction of olivine megacrysts, sample ME02. (b) Photomicrograph (plain light) of dunite mylonite showing strong foliation defined by fine grained, localized shear zones and coarse, sheared olivine porphyroclasts, sample MS001.

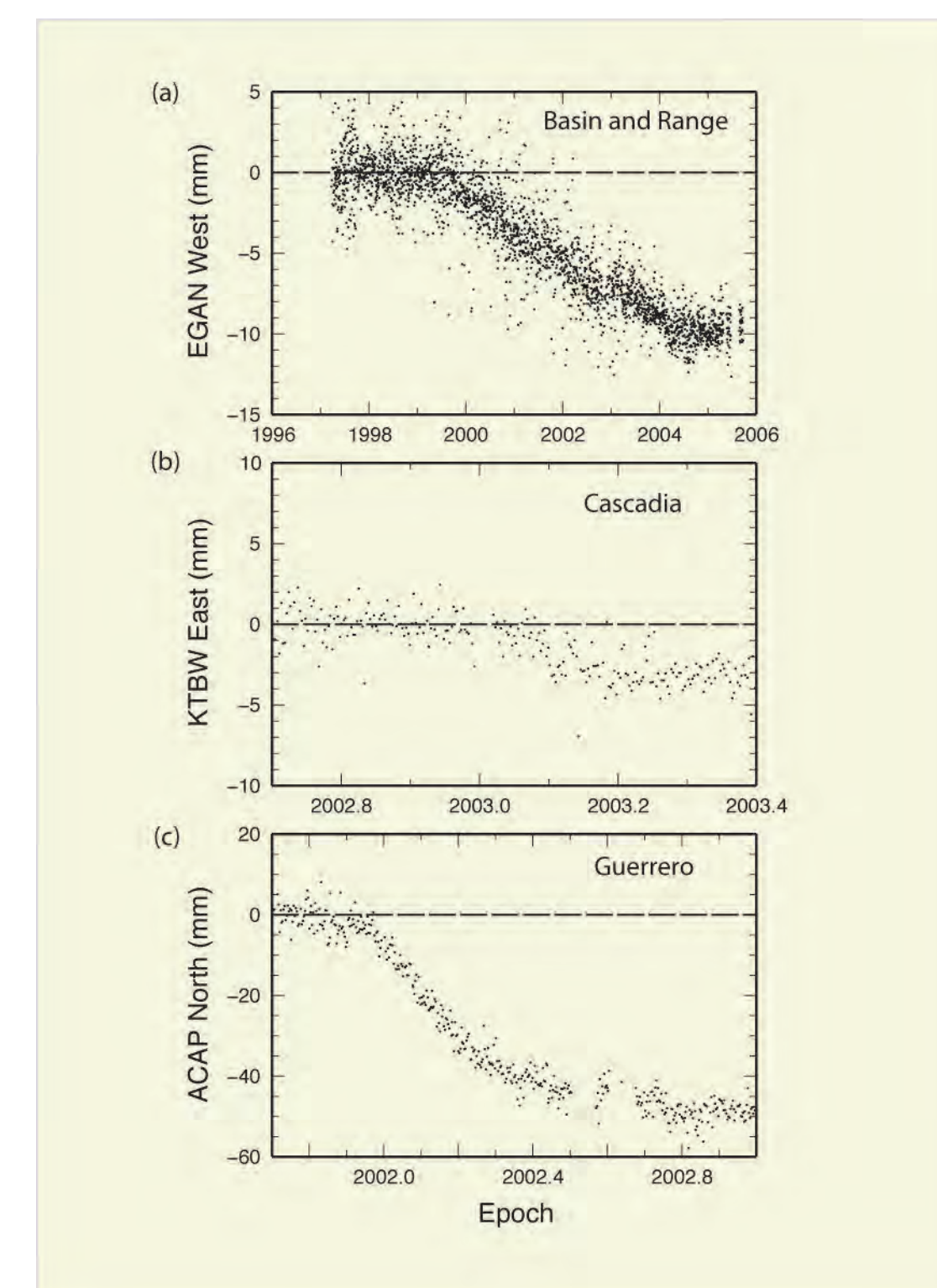


Figure 11. Filtered, detrended time series for (a) east component of baseline EGAN-FOOT, (b) longitude of Cascadia site KTBW during the early 2003 slow earthquake [Melbourne et al., 2005], and (c) latitudinal position of site ACAP during Guerrero silent earthquake of 2001-2002 [Kostoglodov et al., 2003]. Reference frame (zero motion) is established by linear regression through the individual time series between the identified strain events. Note differences in displacements

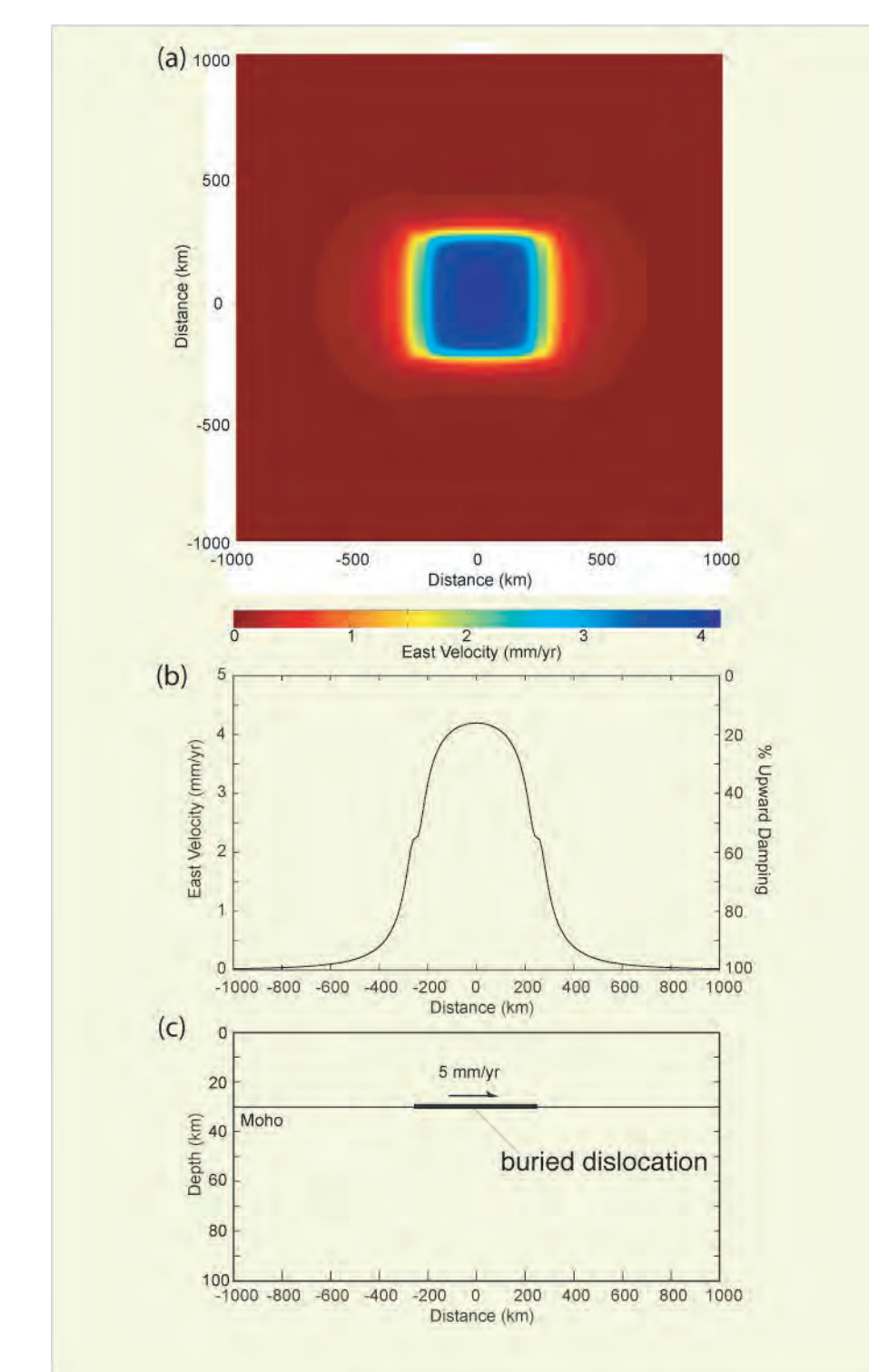


Figure 12. (a) Map of surface horizontal velocity anomaly for 500 km x 500 km horizontal dislocation buried at a depth of 30 km slipping uniformly at 5 mm/yr due east, using the method of Okada (1992). (b) Plot showing horizontal velocity anomaly versus position in the direction of slip at mid-point of the model, parameterized as surface velocity (left axis, mm/yr) and upward damping of horizontal velocity (right axis, percent of slip along dislocation). (c) cross-section of dislocation plane (heavy line) and sense of shear (arrow).

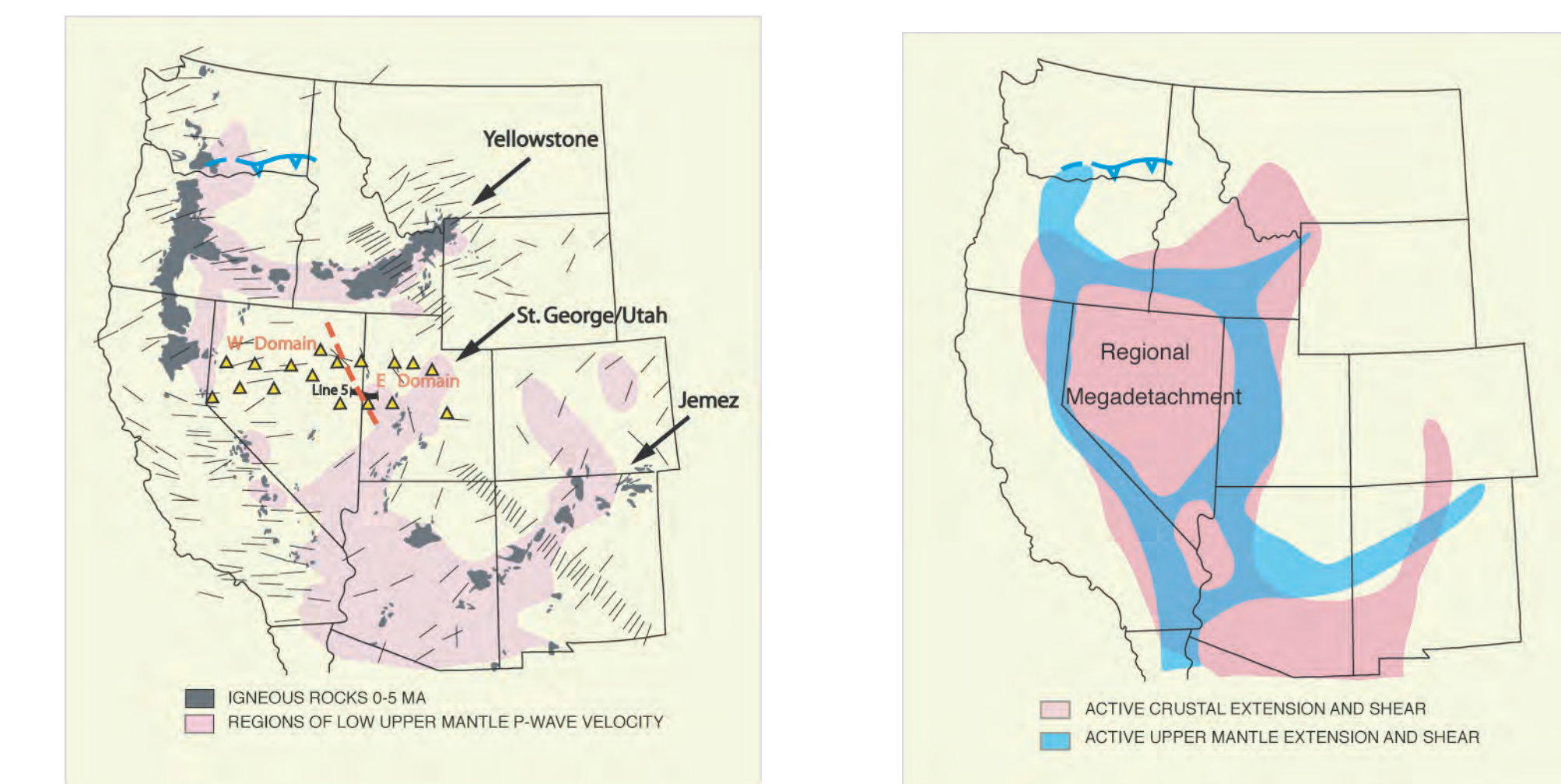


Figure 8. (a) Map showing BARGEN sites from Figure 2 (yellow triangles), the distribution of volcanic rocks younger than 5 Ma (black) after Leudke and Smith [1984], areas of slow P wave velocity (<~1% average) at 100 km depth (pink) after Dueker et al. [2001] and Humphreys and Dueker (1994), orientations of fast S-direction (short, thin red lines; magnitude not indicated) after Savage and Sheehan [2000]; lack of orientation data in east-central Nevada reflects isotropy. (b) Map showing the distribution of Late Cenozoic upper crustal extension compared with the distribution of extension of the subcrustal lithosphere based inferred from magmatism and slow P-wave velocity.

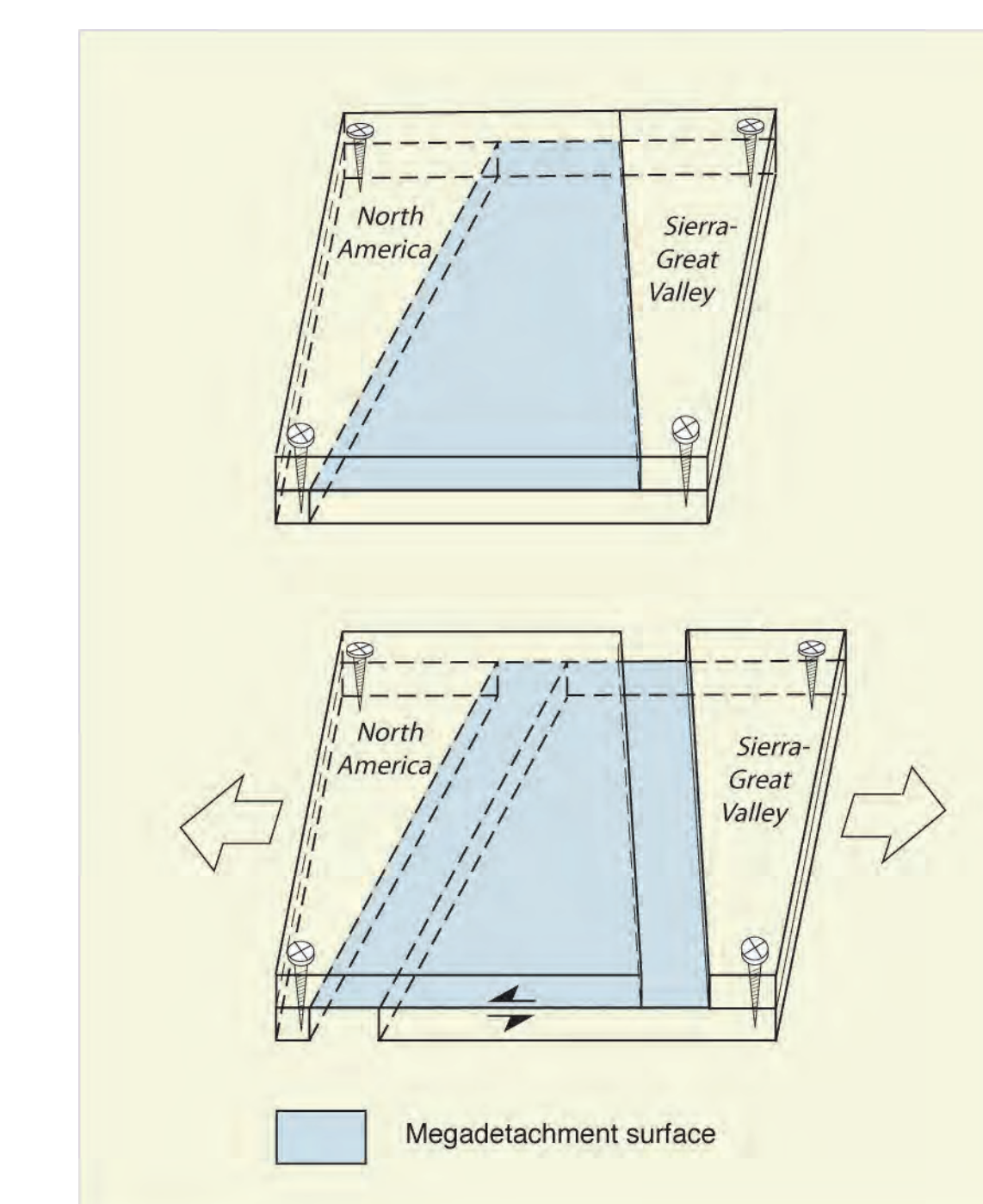


Figure 13. Schematic three-dimensional, strain-compatible model showing the role of the megadetachment in accommodating discordant strain patterns between differently oriented crust and upper mantle extension zones during slip on the detachment. Model neglects strike-slip component of Great-Valley-North America motion, which is presumably focused along the right-hand margin of the megadetachment zone (Figure 14).

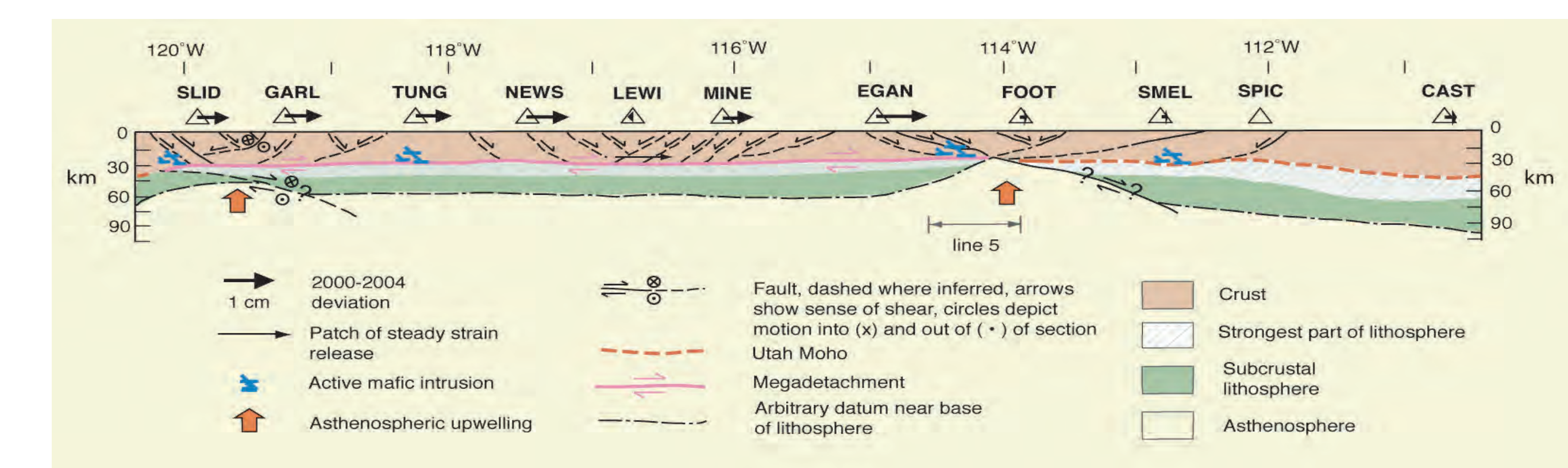


Figure 14. Cross-sectional tectonic model summarizing primary function of the megadetachment and its relationship to active structures in the upper crust and inferred structures in the upper mantle. Section is constructed using interpretations along the COCORP 40°N profile (Figure 1) and data discussed in text.

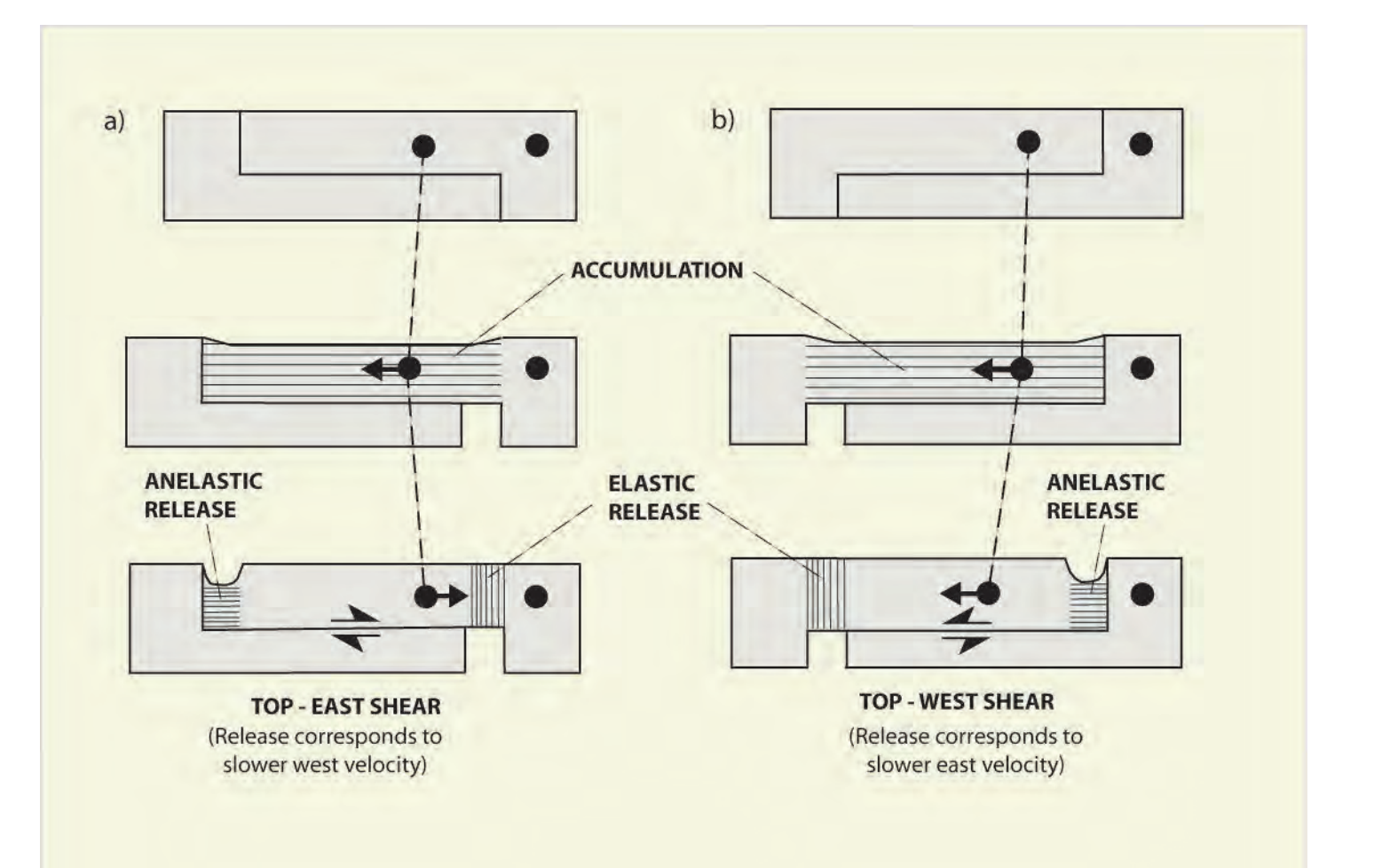


Figure 9. Schematic east-west cross-sectional models (not to scale) illustrating two possible strain release modes for the megadetachment discussed in text. (a) strain release top-east, implying faulting in western Nevada is transferred to subcrustal lithospheric extension in west.

¹Division of Geological and Planetary Sciences, California Institute of Technology, Pasadena, California, USA
²Harvard-Smithsonian Center for Astrophysics, Cambridge, Massachusetts, USA
³Department of Geological Sciences, University of Michigan, Ann Arbor, Michigan, USA
⁴Now at: Department of Earth Science, Rice University, Houston, Texas, USA
⁵Now at: Department of Earth and Space Science and Engineering, York University, Toronto, Canada